Supporting Information

Role of Cerebellar GABAergic Dysfunctions in the Origins of Essential Tremor

Xu Zhang, Sabato Santaniello

Biomedical Engineering Department, University of Connecticut, Storrs, CT (USA)

SI Note 1: Mathematical Descriptions of the CCTC Network Model

The inferior olivary nucleus (ION) neuron model was modified from ref. (3) by including the somatic compartment and replacing the model of calcium channel with the model provided in refs. (4, 5). The deep cerebellar neuron (DCN) model was the somatic compartment of the original model proposed in ref. (6). The nucleo-olivary neuron (NO) model was modified from the DCN model by preserving the fast sodium current (I_{NaF}), the fast and slow delayed rectifier potassium currents (I_{fKdr} and I_{sKdr}, respectively), and the leaky channel, as in ref. (8). The equations of the remaining neuron models in the network are as in refs. (9-12). The temperature parameters, if included in the original models, were adjusted to physiological temperature (36 °C).

Each ION neuron received a different offset current (I_{OC}, *Table S1*) to generate subthreshold oscillations with slightly different intrinsic frequencies. Similarly, each Purkinje cell (PC) was endowed with a different I_{OC} to simulate a range of spontaneous firing rates. The DCN and NO neurons, the pyramidal neurons (PYN), and the fast-spiking interneurons (FSI), instead, received a constant I_{OC} specific to the neuron type to match their baseline firing rates reported in refs. (8, 12-14). For each neuron except those in the granular layer (GrL), a membrane noise $w_m(t) \sim \mathcal{N}(0, \sigma_m^2)$ was added to the capacitive current term of the Hodgkin-Huxley equation to induce a moderate level of stochasticity. A full list of the modified parameters is reported in *Table S1*. Other parameters, instead, are as reported in refs. (3, 4) (ION neurons), (9) (PCs), (6) (DCN and NO neurons), (10) (GrL neurons), (11) (thalamocortical [TC] neurons, used in Vim), and (12) (PYNs and FSIs). *Fig. S1* shows that the modified models for ION, DCN, and NO neurons matched the dynamics of neurons recorded

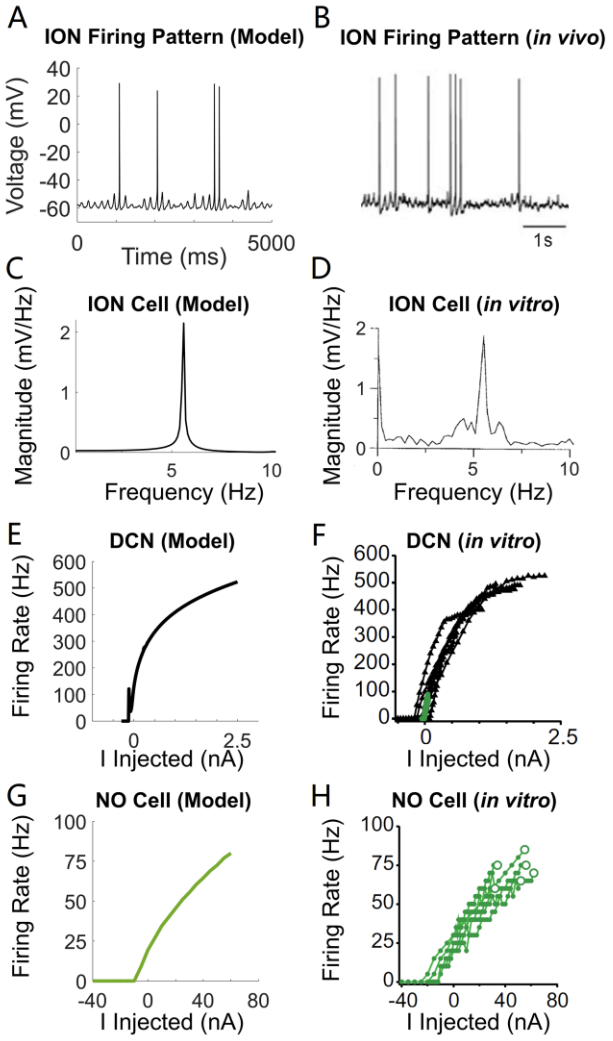

Figure S1. Single-unit activity of inferior olivary (ION), deep cerebellar (DCN), and nucleo-olivary (NO) neurons in the proposed model (A, C, E, G) and in single unit recordings from animals (B, D, F, H). **A-B)** Membrane voltage trace of a neuron in the inferior olivary nucleus under normal conditions in the model (A) and single-unit *in vivo* recording from guinea pigs (B). **C-D)** Average power spectral density (PSD) of the membrane potential of a single ION model neuron under normal, tremor-free conditions (C) (simulation: 10,000 ms) and of a single-unit *in vitro* recording in the inferior olivary nucleus of guinea pigs (D). **E-H)** Current-frequency (*I-f*) curve for DCN (E, F) and NO (G, H) neurons under a range of offset currents in the proposed model (E, G) and *in vitro* in a mouse model under anesthesia (F, H). Fig. S1B: Republished with permission of the Society for Neuroscience, from ref. (1); permission conveyed through Copyright Clearance Center, Inc. Fig. S1D: Reprinted from ref. (7), with permission from Elsevier. Fig. S1F and Fig. S1H: Republished with permission of the Society for Neuroscience, from ref. (8); permission conveyed through Copyright Clearance Center, Inc.

in animal preparations (ION: guinea pig; DCN and NO: mouse). Specifically, the ION neuron model was characterized by a sustained subthreshold oscillatory activity with frequencies ranging between 5.38 Hz and 5.78 Hz, depending on the value of I_{OC}, which matches the range of spontaneous subthreshold oscillations observed *in vitro* in slices including the ION (7), see *Fig. S1*, panels A-D. Similarly, the proposed models for DCN and NO neurons matched the *I-f* curve estimated *in vivo* in mice under anesthesia (8), *Fig. S1*, panels E-H.

Fig. S2, panels A and C, show the sample distribution of inter-spike intervals (ISI) for a Purkinje cell (PC) and the deep cerebellar neuron (DCN), respectively, in one instance of the CCTC model. Parameters of the interconnections between DCN and PCs were constrained to match the sample ISI distribution of PC and DCN recorded *in vivo* in healthy non-human primates during voluntary arm movements, see *Fig. S2*, panels B and D.

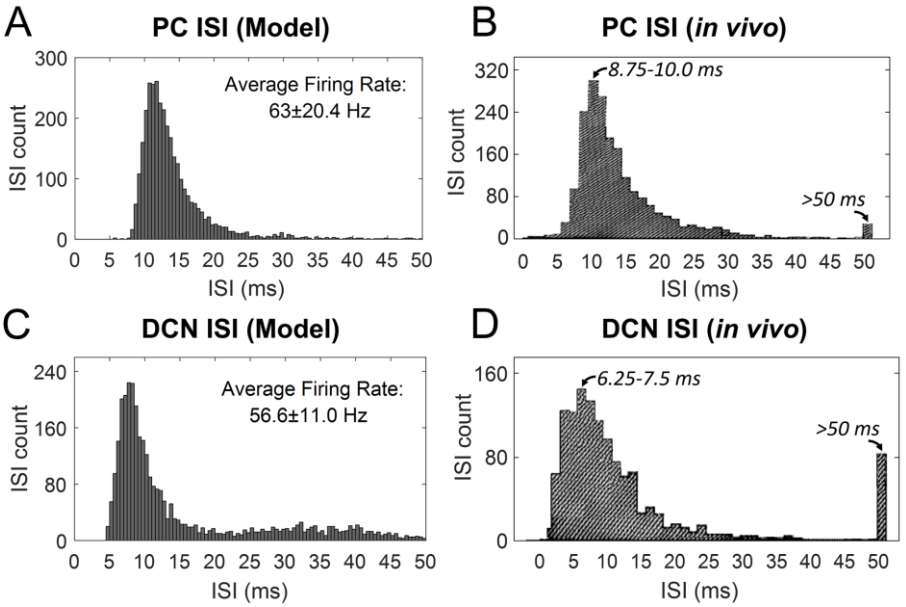

Figure S2. A-D) Inter-spike interval (ISI) distribution of one Purkinje cell (PC) and one deep cerebellar neuron (DCN) in the CCTC model (A, C) and in awake nonhuman primates (B, D) during upper limb movements. Histograms in A) and C) are from one instance of the CCTC model simulated over a 60,000-ms-long period. *Inset*: Average firing rate (mean ± S.D.) of the PCs and DCNs, respectively, across three instances of the CCTC model, each instance simulated over a 60,000-ms-long period. Fig. S2B and Fig. S2D: Reprinted with permission from ref. (2); permission conveyed through Copyright Clearance Center, Inc.

Network Connectivity. A simplified representation of the thalamocortical pathway is included in our model, with one thalamocortical (TC) neuron in the Vim projecting onto six, randomly chosen PYNs and both FSIs, and four PYNs projecting back to the TC neuron. In addition, four, randomly chosen PYNs project individually onto four identical GrL structures, representing the relay of cortical inputs to the cerebellum via pontine nuclei (15). All PYNs project onto the DCN to simulate the formation of extensive mossy fiber excitation, as reported in ref. (16). The NO neuron model, instead, does not receive excitatory input from the PYNs to account for the low *in vivo* firing activity of the nucleo-olivary neurons (17, 18). Also, a total of 8 out of 20 PYNs are neither involved in connections with the Vim nor with the cerebellar cortex and are used to account for the important fact that thalamocortical and cortico-cerebellar projections may target different cortical layers. Each ION neuron projects onto five PCs without overlapping as reported in ref. (19). One of the IONs projects onto the DCN to account for the presence of climbing fiber collaterals. These collaterals are known to produce small, short-latency activation of DCN neurons following a spike of the ION neurons (13, 20, 21).

Fig. S3 on next page reports the interconnections between ION neurons in the inferior olivary nucleus (*Fig. S3*, panel A), the motor cortex (*Fig. S3*, panel B), and the neurons forming the granular layer (GrL complex) in the cerebellar cortex (*Fig. S3*, panel C). The topology of the resultant neuronal networks is consistent with anatomical considerations reported in ref. (10). The olivocerebellar pathway formed by PCs, NO, and ION neurons represents a loop, as indicated in ref. (22), and the di-synaptic excitatory pathway from the DCN to the ION neurons, i.e., the dentato-rubro-olivary pathway, is organized to form the Guillain-Mollaret triangle (23).

Synapses between the granule cells, Golgi cells, and stellate cells in the GrL complex were modeled as in ref. (8). Synapses within the motor cortex as well as those between the PCs and DCN or NO neurons, instead, were modeled as follows:

$$I_{syn} = g_{syn} s\left(V_i(t) - E_{syn}\right) \tag{1}$$

$$\frac{ds}{dt} = \alpha\left[1 + \tanh\left(\frac{V_j(t-\Delta t) - V_{off}}{\beta}\right)\right](1-s) - \frac{s}{\tau} + w_s(t) \tag{2}$$

where $V_j(t - \Delta t)$ is the membrane potential of the pre-synaptic neuron at time $(t - \Delta t)$ and Δt accounts for the synaptic transmission delay. The term $w_s(t)$ represents synaptic noise and is defined by:

$$\frac{dw_s(t)}{dt} = S, S \sim \mathcal{N}(0, \sigma_s^2) \tag{3}$$

where $\mathcal{N}$ is a Gaussian distribution with mean 0 and standard deviation σ_s. For the motor cortex, V_{off} =0 mV, β=4, Δt=0, and the rest of the parameters were set as described in ref. (24). For the synapses between PCs and DCN or NO neurons, the parameters are reported in *Table S2*.

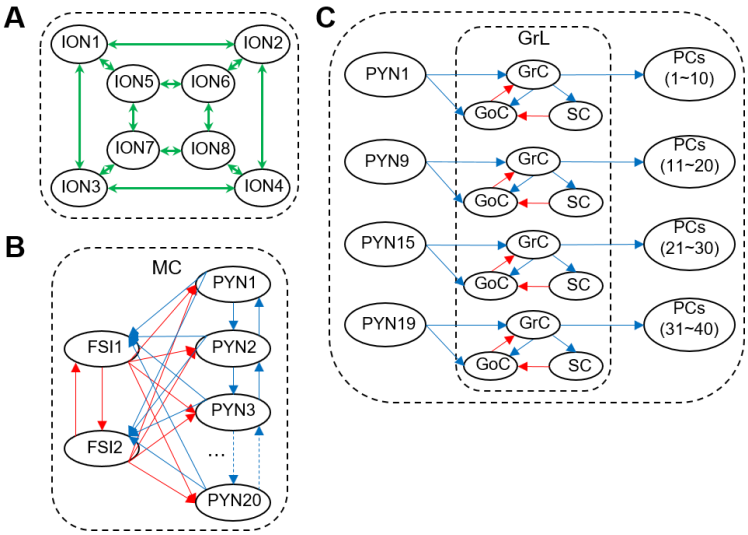

Figure S3. **A-C)** Schematic of the network connections within the inferior olivary nucleus (A), the motor cortex [MC] (B), and the granular layer [GrL] (C). Green arrows in A) indicate electric gap junctions, whereas blue and red arrows in B-C) indicate glutamatergic excitatory and GABAergic inhibitory connections, respectively. Arrow tips indicate post-synaptic neurons.

All the remaining synapses along the CCTC loop were simulated in NEURON using the NETCON mechanism, which produces an event-based post-synaptic current upon detection of a presynaptic spike, and speeds up the simulation (25). NETCON mechanisms were specifically used to model the di-synaptic connections DCN→ ION, PYN→DCN, and PYN→GrL, as well as the di-synaptic inhibitory connection between ION neurons and PCs mediated by cerebellar interneuron (26). A NETCON mechanism works as follows: denoted with *i* and *j* the post-synaptic target neuron and the pre-synaptic neuron, respectively, NETCON delivers a post-synaptic current I_{syn} to the target neuron *i* in response to the occurrence of a spike in the pre-synaptic neuron *j*. The current I_{syn} is either an exponentially decaying current of form:

$$I_{syn} = g_{syn}(e^{-(t-\Delta t)/\tau^{j\to i}} + w_s(t))\left(V_i - E_{syn}\right) \tag{4}$$

or a two-state exponentially decaying current of form:

$$I_{syn} = \frac{A \cdot g_{syn}}{\tau_2^{j\to i} - \tau_1^{j\to i}}\left[\left(e^{-(t-\Delta t)/\tau_2^{j\to i}} - e^{-(t-\Delta t)/\tau_1^{j\to i}}\right) + w_s(t)\right]\left(V_i - E_{syn}\right) \tag{5}$$

where Δt is the synaptic transmission delay from neuron *j* to neuron *i*, E_{syn} is the synaptic reverse potential, V_i is the postsynaptic membrane potential in neuron *i*, g_{syn} is the postsynaptic conductance, and $\tau_k{}^{j\to i}$, k=1, 2, are decay time constants, respectively. A spike was detected in the pre-synaptic neuron *j* if the voltage V_j passed the threshold *thr*= –40 mV (–50 mV for Golgi cells).

To simulate the spontaneous discharge activity of the pyramidal neurons in the motor cortex, each PYN received post-synaptic currents triggered by a train of randomly generated pre-synaptic spikes (Poisson process). The parameter λ of the Poisson processes (i.e., average inter-event interval) was randomly generated (one Poisson process per PYN) according to a Gaussian distribution, i.e., $\lambda \sim \mathcal{N}(\mu, \sigma^2)$ with μ=20 ms and σ=5 ms. Similarly, the spontaneous discharge activity of the ION neurons was simulated by delivering post-synaptic currents to these neurons in response to a train of randomly generated pre-synaptic spikes (Poisson process). The parameter λ of the Poisson processes was randomly generated (one Poisson process per ION) and followed a uniform distribution, i.e., $\lambda \sim \mathcal{U}(350, 650)$ ms, to match experimental data in ref. (27). All the parameters used in the synapses in our model are reported in *Table S2*.

Each ION neuron was connected to three additional ION neurons via gap junctions to reproduce quantitative neuroanatomical indications reported ref. (27), see *Fig. S3*, panel A. Each gap junction was simulated as a linear function of the membrane potential difference between the connected ION neurons, i.e.,

$$I_{gap} = g_{gap}\gamma_C\left(V_i - V_j\right) \tag{6}$$

where γ_C is a coupling coefficient, g_{gap} is the gap junction conductance, and V_i and V_j are the membrane potential of the target cell i and the cell j in electrotonic contact with the target cell. The conductance g_{gap} was normally distributed across the gap junctions in the model with values drawn from the distribution function $\mathcal{N}(\mu, \sigma^2)$ with parameters μ=2.25×10^{-5} mS/cm^2 and σ=1.0×10^{-5} mS/cm^2 to match data in ref. (27).

The coupling coefficient γ_C was defined as a scalar ranging between 0 and 1 and was used to describe the effects of the nucleo-olivary activity onto the inferior olivary neurons. It has been reported, in fact, that the NO neurons project onto both the soma and the gap junctions of the ION neurons, which results in a strong decoupling between the ION neurons and a significant hyperpolarization of the ION somas (27). To account for the effects of the NO neurons onto the gap junctions, we modeled the coefficient γ_C as a function of the spiking of the NO neuron, i.e.:

$$\gamma_C = 1 - 0.9\tanh\left(S\left(t\right)\right) \tag{7}$$

where $S(t)$ is a two-state exponential function of the NO spiking time, i.e.:

$$S(t) = \frac{A \cdot s}{\tau_2 - \tau_1}\left(e^{-t/\tau_2} - e^{-t/\tau_1}\right). \tag{8}$$

Specific parameters for the gap junctions are reported in *Table S2*. The innervation of the climbing fibers to the Purkinje cells (PCs) was simulated by introducing AMPA-mediated and NMDA-mediated glutamatergic synapses on the PCs. The values of these currents match the synaptic currents reported in refs. (28-31). The interneuron-mediated inhibitory effects of the ION spiking onto the PCs (26) were modeled through a NETCON mechanism (parameters are in *Table S2*). *Fig. S4* on next page illustrates the spiking pattern of the neuron models in the proposed CCTC loop before and after the application of a single, depolarizing impulse to the ION neurons (red vertical line). Neurons from the motor cortex (PYNs and FSIs) were mildly affected by the GABAergic disfunctions in cerebellum (*Fig. S4*, panels A-B). PCs and GrL neurons, instead, responded tonically to the simultaneous activation of the ION neurons. This activation was triggered externally (red vertical line) and engaged a single response under normal, tremor-free conditions (*Fig. S4*, panels C and E). Under ET conditions, instead, the simultaneous activation of the ION neurons elicited a sustained oscillation that outlasted the effects of the impulse and spread through all the cerebellar neurons, see *Fig. S4*, panels D and F. The ET conditions correspond to the GABAergic dysfunctions simulated in Fig. 3B-E in the main text, i.e., $\mathcal{R}$=0.7 and $\tau^{PC\rightarrow DCN}$=12 ms.

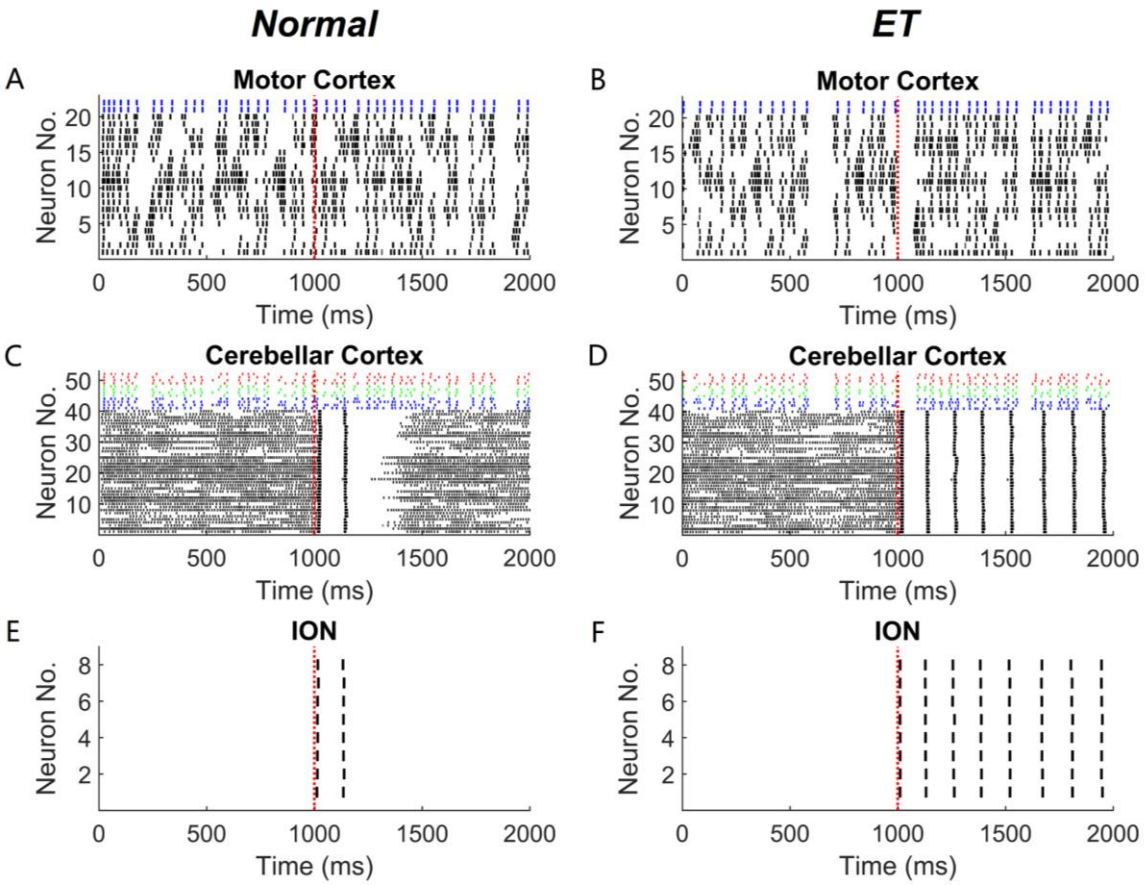

Figure S4. Raster plot of neural populations under normal, tremor-free conditions (A, C, E) and essential tremor (ET) conditions (B, D, F). **A-B)** Raster plot of neuron models from the motor cortex (black: PYNs; blue: FSIs); **C-D)** Raster plot of neuron models from the cerebellar cortex (black: Purkinje cells; blue: Golgi cells; green: granule cells; red: stellate cells. **E-F)** Raster plot of olivary neuron models from the inferior olivary nucleus. In each plot, the red dotted vertical line identifies the time t=1,000 ms when a single supra-threshold (10 pA) current pulse (pulse duration: 20 ms) was applied to all neurons in the inferior olivary nucleus. The CCTC model was simulated for 4,000 ms, integration step: 0.0125 ms.

SI Note 2: Data Analysis

The two-dimensional maps reported in Fig. 3A and Fig. 5B in the main text, and *Fig. S5* on next page were computed from 10,000-ms simulations of three instances of the model with different random seeds for each combination ($\mathcal{R}$, $\tau^{PC\rightarrow DCN}$) obtained by varying $\mathcal{R}$ between 0 and 1 with 0.025 increments and $\tau^{PC\rightarrow DCN}$ between 2.0 ms and 24 ms with 0.5 ms increments. A total of 1,800 grid points ($\mathcal{R}$, $\tau^{PC\rightarrow DCN}$) were considered. The boundaries of the tremor regions were fitted by the sum of two exponential functions. Finally, a 5-point moving average filter was implemented both horizontally and vertically to smooth the maps. Similarly, the two-dimensional map reported in Fig. 4B in the main text was computed for every pair of parameters (I_{STEP}, T), with I_{STEP} ranging between 0.01 pA and 1 pA (resolution: 0.01 pA) and T ranging between 10 ms and 180 ms (resolution: 1 ms), thus resulting in 17,100 grid points. For each parameter pair, three model instances were simulated for 6,000 ms and the ION spiking rate was calculated as the average firing rate of any ION that sustained spiking over the entire simulation period.

Rate, Burst, and Power Spectral Analyses. The firing rates of individual neurons reported in section 2.1 in the main text and *Fig. S2* (insets) were calculated from three model instances, each one simulated over a simulation period of 60,000 ms under normal tremor-free condition (the first 1,000 ms was discarded to let the network model reach steady-state conditions). The firing rates were reported as mean ±

S.D. evaluated over non-overlapping 1,000-ms-long segments of simulated data. In the subsequent analyses, a burst was defined as a group of at least three consecutive spikes with inter-spike interval no more than 30 ms. The burst detection was implemented using the method in ref. (32).

The power spectral density (PSD) of the neurons in Fig. 2E in the main text was computed from spike trains recorded over 60,000-ms-long simulations. Spike trains were sampled at 800 Hz and the PSD was computed using the Welch's method as average over 4,000-ms-long windows (Hanning window, 2,000-ms overlap). Three model instances were simulated and the resultant thalamocortical spike trains were used.

The power spectrogram in Fig. 6A and Fig. 6H in the main text were computed via wavelet decomposition (Morlet wavelet) on the superposition of the spike trains of 5 TC neurons in the Vim.

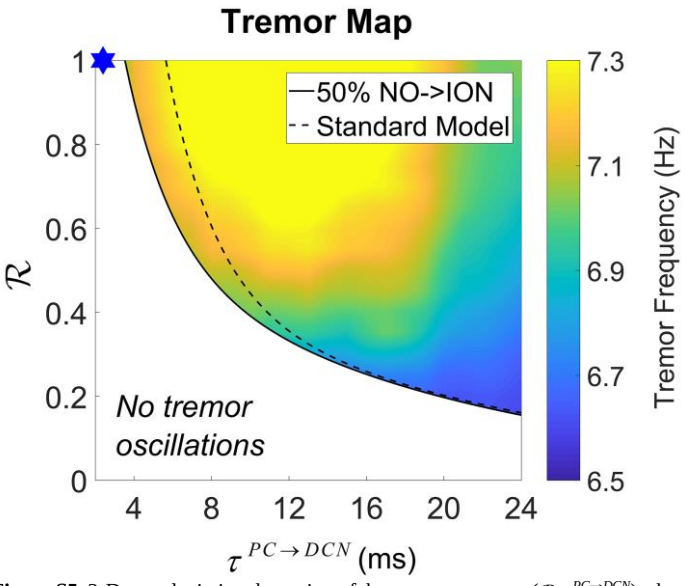

Figure S5. 2-D map depicting the region of the parameter space ($\mathcal{R}$, $\tau^{PC\rightarrow DCN}$) where tremor activity in the Vim is observed along with the tremor frequency (colormap). The tremor frequency was defined as the frequency of maximum power spectrum density of the Vim, and the blue mark indicates parameters used to simulate normal, tremor-free conditions. The synaptic strength of the NO→ION synapses in this figure was reduced to 50% of the original value used in Fig. 3A in the main text. The dashed line indicates the boundary of the tremor map reported in Fig. 3A in the main text for the original model (*Standard Model*). Note that the average tremor frequency increased by ~0.3 Hz across the entire map over the value in Fig. 3A.

SI Note 3: Connectivity of the Scale-Up Version of the CCTC Model

The 85-single compartment CCTC model was scaled up by a factor 5, i.e., the number of single compartment neurons in each neural population represented in the model was increased five times, thus resulting in a 425-single compartment CCTC model, which included 40 ION neurons, 200 PCs, 5 DCN and 5 NO neurons, 5 TC neurons in the Vim, 100 PYNs, 10 FSIs, and 20 GrL clusters altogether. Three instances of this scaled-up CCTC model were simulated with different random seeds. For each instance, the following rules were used to randomize the connectivity between the thalamocortical and olivocerebellar systems:

1) The ION neurons were divided in 5 groups (i.e., 8 neurons per group), each group forming a closed ring as depicted in *Fig. S3*, panel A. Four out of 8 ION neurons in each group formed gap junctions with ION neurons from neighboring instances, 2 on each side. For instance, ION neurons 1 and 3 in one group formed gap junctions with ION neurons 2 and 4, respectively, from a neighboring group, and vice versa. The gap junction conductance g_{gap} was increased by 50% to compensate for the more extensive inter-group connections. ION neurons in one group shared the same presynaptic Poisson process source input, see PP→ION synapses in *Table S2*;

2) Each group of ION neurons cumulatively targeted M PCs, where $30 \leq M \leq 50$ and M was drawn from a Gaussian distribution function with mean μ=40 and S.D. σ=4. Within an ION group, each ION neuron projected simultaneously onto K randomly chosen PCs out of the M PCs, where the value K was drawn from a Gaussian distribution with mean μ=5 and S.D. σ=2. This guaranteed that every ION neuron projected onto a different number K of PCs, with $1 \leq K \leq 10$;

3) Every DCN in the model received GABAergic projections from W out of 200 PCs, where the value

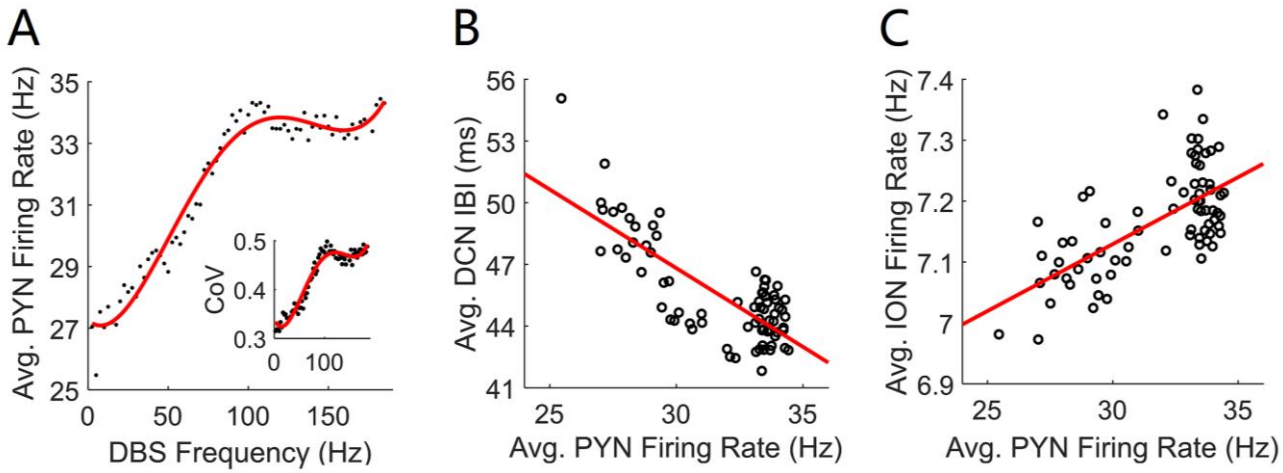

Figure. S6. A) Average firing rate for the pyramidal neurons (PYNs) in response to Vim DBS at different frequencies (black circles) and the least-square fourth order polynomial fit (red curve, coefficient of determination for the fitting R^2=0.96). *Inset*: Coefficient of variation (CoV) of the PYN firing rates in response to the Vim DBS (black dots) and least-square fourth order polynomial fit (red curve, R^2=0.95). **B-C)** Linear regressor (red line) estimated for the average DCN inter-burst intervals (R^2=0.61) (B) and the average ION firing rate (R^2=0.43) (C) as a function of the average PYN firing rate under Vim DBS from A) (black circles). Each data point in A-C) was obtained from a 5,000-ms simulation of the CCTC model under the ET condition with parameters $\mathcal{R}$=0.7 and $\tau^{PC\rightarrow DCN}$=12 ms. First 1,000 ms were discarded to let model instances reach steady-state conditions.

W was drawn from a Gaussian distribution with mean μ=40 and S.D. σ=4 for every DCN. This guaranteed that every DCN received from a different number W of PCs, with $30 \leq W \leq 50$ PCs. Each NO neuron, instead, received GABAergic inputs from 40 PCs. The Purkinje cells projecting onto a DCN or NO neuron were selected randomly.

4) Every DCN projected di-synaptically onto W_1 out of 40 ION neurons chosen randomly, where W_1 was drawn from a Gaussian distribution with mean μ=40 and S.D. σ=4 and varied for every DCN. In this way, we maximized the inter-loop connections by allowing that ION neurons from different groups may receive from the same DCN;

5) Every DCN cell projected onto a TC neuron in the Vim (ratio 1:1); every TC neuron projected onto 6 PYNs and received glutamatergic inputs from 4 PYNs with no overlapping;

6) Every PYN formed glutamatergic projections with 5 neighboring PYNs. The synaptic strength g_{syn} of the PYN→PYN connections was reduced to 20% of the original value reported in *Table S2* to accommodate for the increased number of projections. Each FSI received glutamatergic inputs from all 100 PYNs, and GABAergic inputs from the remaining 9 FSIs. Similarly, the synaptic strengths g_{syn} of the PYN→FSI and FSI→FSI connections were reduced to 20% and 11.1% of the original values reported in *Table S2*, respectively. Finally, the FSIs formed GABAergic projections onto all 100 PYNs, and the synaptic strength g_{syn} of the FSI→PYN connections was reduced to 10% of the original value in *Table S2*;

7) Every DCN received glutamatergic inputs from 20 randomly chosen PYNs. Similarly, every GrL complex received inputs from 4 randomly chosen PYNs without overlapping and projected onto 10 PCs. The PYNs projecting onto the GrL or DCN neurons did not necessarily receive input from the TC neurons in the Vim;

8) To reflect the heterogeneous properties across the 200 PC→DCN synapses, we modeled the normal, tremor-free condition by setting the parameters $\tau^{PC\rightarrow DCN} \sim \mathcal{N}(\mu, \sigma^2)$, μ=2.4 ms, σ=0.4 ms, and $\mathcal{R} \sim \mathcal{N}(\mu, \sigma^2)$, μ=1, σ=0.2, and we modeled the ET condition by setting $\tau^{PC\rightarrow DCN} \sim \mathcal{N}(\mu, \sigma^2)$, μ=12 ms, σ=2 ms, and $\mathcal{R} \sim \mathcal{N}(\mu, \sigma^2)$, μ=0.7, σ=0.14.

SI References.

1. Chorev E, Yarom Y, & Lampl I (2007) Rhythmic episodes of subthreshold membrane potential oscillations in the rat inferior olive nuclei in vivo. *J Neurosci* 27(19):5043-5052.
2. Thach WT (1968) Discharge of Purkinje and cerebellar nuclear neurons during rapidly alternating arm movements in the monkey. *J Neurophysiol* 31(5):785-797.
3. Schweighofer N, Doya K, & Kawato M (1999) Electrophysiological properties of inferior olive neurons: A compartmental model. *J Neurophysiol* 82(2):804-817.
4. Manor Y, Rinzel J, Segev I, & Yarom Y (1997) Low-amplitude oscillations in the inferior olive: a model based on electrical coupling of neurons with heterogeneous channel densities. *J Neurophysiol* 77(5):2736-2752.
5. Torben-Nielsen B, Segev I, & Yarom Y (2012) The generation of phase differences and frequency changes in a network model of inferior olive subthreshold oscillations. *PLoS Comput Biol* 8(7):e1002580.
6. Steuber V, Schultheiss NW, Silver RA, De Schutter E, & Jaeger D (2011) Determinants of synaptic integration and heterogeneity in rebound firing explored with data-driven models of deep cerebellar nucleus cells. *J Comput Neurosci* 30(3):633-658.
7. Lampl I & Yarom Y (1997) Subthreshold oscillations and resonant behavior: two manifestations of the same mechanism. *Neuroscience* 78(2):325-341.
8. Najac M & Raman IM (2015) Integration of Purkinje cell inhibition by cerebellar nucleo-olivary neurons. *J Neurosci* 35(2):544-549.
9. Akemann W & Knopfel T (2006) Interaction of Kv3 potassium channels and resurgent sodium current influences the rate of spontaneous firing of Purkinje neurons. *J Neurosci* 26(17):4602-4612.
10. Garrido JA, Ros E, & D'Angelo E (2013) Spike timing regulation on the millisecond scale by distributed synaptic plasticity at the cerebellum input stage: a simulation study. *Front Comput Neurosci* 7(64):64.
11. Meijer HG, *et al.* (2011) From Parkinsonian thalamic activity to restoring thalamic relay using deep brain stimulation: new insights from computational modeling. *J Neural Eng* 8(6):066005.
12. Destexhe A, Contreras D, & Steriade M (1998) Mechanisms underlying the synchronizing action of corticothalamic feedback through inhibition of thalamic relay cells. *J Neurophysiol* 79(2):999-1016.
13. Najac M & Raman IM (2017) Synaptic excitation by climbing fibre collaterals in the cerebellar nuclei of juvenile and adult mice. *J Physiol* 595(21):6703-6718.
14. Raman IM, Gustafson AE, & Padgett D (2000) Ionic currents and spontaneous firing in neurons isolated from the cerebellar nuclei. *J Neurosci* 20(24):9004-9016.
15. Sasaki K, Kawaguchi S, Shimono T, & Prelevic S (1970) Electrophysiological studies of the pontine nuclei. *Brain Res* 20(3):425-438.
16. Wu Y & Raman IM (2017) Facilitation of mossy fibre-driven spiking in the cerebellar nuclei by the synchrony of inhibition. *J Physiol* 595(15):5245-5264.
17. Bazzigaluppi P, Ruigrok T, Saisan P, De Zeeuw CI, & de Jeu M (2012) Properties of the nucleo-olivary pathway: an in vivo whole-cell patch clamp study. *PLoS One* 7(9):e46360.
18. Uusisaari M & De Schutter E (2011) The mysterious microcircuitry of the cerebellar nuclei. *J Physiol* 589(Pt 14):3441-3457.
19. Eccles JC, Llinas R, & Sasaki K (1966) The excitatory synaptic action of climbing fibres on the Purkinje cells of the cerebellum. *J Physiol* 182(2):268-296.
20. Hoebeek FE, Witter L, Ruigrok TJ, & De Zeeuw CI (2010) Differential olivo-cerebellar cortical control of rebound activity in the cerebellar nuclei. *Proc Natl Acad Sci U S A* 107(18):8410-8415.
21. Lu H, Yang B, & Jaeger D (2016) Cerebellar Nuclei Neurons Show Only Small Excitatory Responses to Optogenetic Olivary Stimulation in Transgenic Mice: In Vivo and In Vitro Studies. *Front Neural Circuits* 10:21.

22. Bengtsson F & Hesslow G (2006) Cerebellar control of the inferior olive. *Cerebellum* 5(1):7-14.

23. Murdoch S, Shah P, & Jampana R (2016) The Guillain-Mollaret triangle in action. *Pract Neurol* 16(3):243-246.

24. Santaniello S, *et al.* (2015) Therapeutic mechanisms of high-frequency stimulation in Parkinson's disease and neural restoration via loop-based reinforcement. *Proc Natl Acad Sci U S A* 112(6):E586-595.

25. Hines ML & Carnevale NT (2004) Discrete event simulation in the NEURON environment. *Neurocomputing* 58:1117-1122.

26. Mathews PJ, Lee KH, Peng Z, Houser CR, & Otis TS (2012) Effects of climbing fiber driven inhibition on Purkinje neuron spiking. *J Neurosci* 32(50):17988-17997.

27. Lefler Y, Yarom Y, & Uusisaari MY (2014) Cerebellar inhibitory input to the inferior olive decreases electrical coupling and blocks subthreshold oscillations. *Neuron* 81(6):1389-1400.

28. Otis TS, Kavanaugh MP, & Jahr CE (1997) Postsynaptic glutamate transport at the climbing fiber-Purkinje cell synapse. *Science* 277(5331):1515-1518.

29. Burroughs A, *et al.* (2017) The dynamic relationship between cerebellar Purkinje cell simple spikes and the spikelet number of complex spikes. *J Physiol* 595(1):283-299.

30. Murphy JT & Sabah NH (1970) The inhibitory effect of climbing fiber activation on cerebellar purkinje cells. *Brain Res* 19(3):486-490.

31. Zucca R, Rasmussen A, & Bengtsson F (2016) Climbing Fiber Regulation of Spontaneous Purkinje Cell Activity and Cerebellum-Dependent Blink Responses(1,2,3). *eNeuro* 3(1):ENEURO. 0067-0015.2015.

32. Bakkum DJ, *et al.* (2013) Parameters for burst detection. *Front Comput Neurosci* 7:193.

33. Turecek J, Han VZ, Cuzon Carlson VC, Grant KA, & Welsh JP (2016) Electrical Coupling and Synchronized Subthreshold Oscillations in the Inferior Olive of the Rhesus Macaque. *J Neurosci* 36(24):6497-6502.

34. Sugihara I, Lang EJ, & Llinas R (1993) Uniform olivocerebellar conduction time underlies Purkinje cell complex spike synchronicity in the rat cerebellum. *J Physiol* 470(1):243-271.

35. Davie JT, Clark BA, & Hausser M (2008) The origin of the complex spike in cerebellar Purkinje cells. *J Neurosci* 28(30):7599-7609.

36. Bengtsson F, Ekerot CF, & Jorntell H (2011) In vivo analysis of inhibitory synaptic inputs and rebounds in deep cerebellar nuclear neurons. *PLoS One* 6(4):e18822.

37. Tang T, Suh CY, Blenkinsop TA, & Lang EJ (2016) Synchrony is Key: Complex Spike Inhibition of the Deep Cerebellar Nuclei. *Cerebellum* 15(1):10-13.

38. Hoebeek FE, Khosrovani S, Witter L, & De Zeeuw CI (2008) Purkinje cell input to cerebellar nuclei in tottering: ultrastructure and physiology. *Cerebellum* 7(4):547-558.

39. Uno M, Yoshida M, & Hirota I (1970) The mode of cerebello-thalamic relay transmission investigated with intracellular recording from cells of the ventrolateral nucleus of cat's thalamus. *Exp Brain Res* 10(2):121-139.

40. Hua SE & Lenz FA (2005) Posture-related oscillations in human cerebellar thalamus in essential tremor are enabled by voluntary motor circuits. *J Neurophysiol* 93(1):117-127.

41. Ruigrok TJ & Voogd J (1995) Cerebellar influence on olivary excitability in the cat. *Eur J Neurosci* 7(4):679-693.

42. Devor A, Fritschy JM, & Yarom Y (2001) Spatial distribution and subunit composition of GABA(A) receptors in the inferior olivary nucleus. *J Neurophysiol* 85(4):1686-1696.

43. Pasquereau B, DeLong MR, & Turner RS (2016) Primary motor cortex of the parkinsonian monkey: altered encoding of active movement. *Brain* 139(Pt 1):127-143.

44. Isope P & Barbour B (2002) Properties of unitary granule cell-->Purkinje cell synapses in adult rat cerebellar slices. *J Neurosci* 22(22):9668-9678.

45. Mapelli J, Gandolfi D, & D'Angelo E (2010) High-Pass Filtering and Dynamic Gain Regulation Enhance Vertical Bursts Transmission along the Mossy Fiber Pathway of Cerebellum. *Front Cell Neurosci* 4:14.

46. Ito M, Yoshida M, Obata K, Kawai N, & Udo M (1970) Inhibitory control of intracerebellar nuclei by the purkinje cell axons. *Exp Brain Res* 10(1):64-80.

Neuron type	Parameter	Value	Source
ION	Length (μm)	20	Ref. (33)
	Diameter (μm)	20	Ref. (33)
	E_K (mV)	-70	Modified from ref. (3)
	E_{Na} (mV)	55	Ref. (3)
	g_{Kdr} (mS·cm^2)	9	Ref. (3)
	g_{Na} (mS·cm^2)	37	Ref. (3)
	g_h (mS·cm^2)	8e-2	Ref. (3)
	g_{Ca} (mS·cm^2)	0.27	Ref. (5)
	g_l (mS·cm^2)	0.13	Ref. (5)
	I_{OC} (nA)	$I_{OC} \sim \mathcal{U}$(-1.5,-1.15)×1e-3	Set to match the subthreshold oscillatory activity with ref. (7)
	σ_m (nA)	1e-5	
DCN	Length (μm)	65	Set to fit the *f-I* curve reported in ref. (8)
	Diameter (μm)	20.25	Ref. (8)
	E_K (mV)	-70	Modified from ref. (6)
	E_{Na} (mV)	61	Modified from ref. (6)
	g_{NaF} (mS·cm^2)	1.91e-2	Modified from ref. (6)
	I_{OC} (nA)	-5.3e-2	Set to adjust the baseline firing rate to values in refs. (13, 14)
	σ_m (nA)	5e-2	
NO	Length (μm)	200	Set to fit the *f-I* curve reported in ref. (8)
	Diameter (μm)	14.88	Ref. (8)
	g_{Kdr} (mS·cm^2)	2.86e-2	Modified from ref. (6)
	I_{OC} (nA)	-3e-2	Set to adjust the baseline firing rate to values in ref. (8)
	σ_m (nA)	2e-2	
PC	Q_{10}	2.2	Modified from ref. (9)
	I_{OC} (nA)	$I_{OC} \sim$-3e-4 + Γ(0.8,3.7e-3)	Set to adjust the baseline firing rate to values in ref. (9)
	σ_m (nA)	1e-6	
TC	Length (μm)	96	Ref. (12)
	Diameter (μm)	96	Ref. (12)
	σ_m (nA)	0.1	
PYN	I_{OC} (nA)	0.17	Modified from ref. (24)
	σ_m (nA)	0.1	
FSI	I_{OC} (nA)	0.15	Modified from ref. (24)
	σ_m (nA)	0.1	

Table S1. Parameters used in the proposed model. *Legend*: Γ(0.8,3.7e-3) is the gamma function with shape parameter k=0.8 and scale parameter θ=3.7e-3. $\mathcal{U}$(-1.5,-1.15) is the uniform distribution on the interval between the values -1.5 and -1.15.

Synapse	Parameter	Value	Source
ION→PC (AMPA)	$\tau^{ION\rightarrow PC\ (AMPA)}$ (ms)	0.6	Ref. (28)
	E_{syn} (mV)	0	Value used in every excitatory synapse
	Δt (ms)	4	Ref. (34)
	g_{syn} (uS)	4e-3	Set to reproduce the PC response in refs. (29, 35)
	σ_w	5e-9	Set to induce ±0.1 pA synaptic current fluctuation
ION→PC (NMDA)	$\tau_1^{ION\rightarrow PC\ (NMDA)}$ (ms)	2.63	Ref. (28)
	$\tau_2^{ION\rightarrow PC\ (NMDA)}$ (ms)	28	Ref. (28)
	E_{syn} (mV)	0	
	Δt (ms)	4	Ref. (34)
	g_{syn} (uS)	2.5e-3	Set to reproduce the PC response in refs. (29, 35)
	σ_w	5e-9	Set to induce ±0.1 pA synaptic current fluctuation
ION→PC (di-synaptic interneuron-mediated)	$\tau_1^{ION\rightarrow PC\ (LTD)}$ (ms)	5.0	Refs. (30, 31)
	$\tau_2^{ION\rightarrow PC\ (LTD)}$ (ms)	$\sim\mathcal{N}(\mu, \sigma^2)$, μ=80, σ=10	Refs. (30, 31)
	E_{syn} (mV)	-65	Refs. (30, 31)
	Δt (ms)	14	Ref. (34)
	g_{syn} (uS)	1e-2	Refs. (30, 31)
	σ_w	5e-9	Set to induce ±0.1 pA synaptic current fluctuation
ION→DCN	$\tau^{ION\rightarrow DCN}$ (ms)	0.8	Refs. (13, 21)
	E_{syn} (mV)	0	
	Δt (ms)	2.5	Ref. (13)
	g_{syn} (uS)	5e-3	Refs. (13, 20, 21)
	σ_w	1e-10	Set to induce ±2e-3 pA synaptic current fluctuation
PC→DCN	α	0.2	Set to reproduce the DCN response in refs. (20, 36)
	β	1	Set to reproduce the DCN response in refs. (20, 36)
	V_{off} (mV)	-52	Set to accommodate DCN response to PC CS
	$\tau^{PC\rightarrow DCN}$ (ms)	2.4	Refs. (8, 37)
	E_{syn} (mV)	-80	Ref. (6)
	Δt (ms)	4.2	Ref. (38)
	g_{syn} (uS)	1e-3	Set to reproduce the DCN response in refs. (20, 36)
	σ_w	1e-7	Set to induce ±5.5e-5 pA current fluctuation
PC→NO	α	0.2	Same as PC→DCN
	β	1	Same as PC→DCN
	V_{off} (mV)	-52	Same as PC→DCN
	$\tau^{PC\rightarrow NO}$ (ms)	35	Refs. (8, 38)
	E_{syn} (mV)	-80	Estimated from (8)
	Δt (ms)	4.2	Ref. (38)
	g_{syn} (uS)	2.8e-5	Set to adjust the *in vivo* firing rate in ref. (17)
	σ_w	1e-7	Set to induce ±2e-3 pA synaptic current fluctuation
DCN→TC	$\tau_1^{DCN\rightarrow Vim}$ (ms)	1.3	Ref. (39)
	$\tau_2^{DCN\rightarrow Vim}$ (ms)	20	Ref. (39)
	E_{syn} (mV)	0	
	Δt (ms)	2	Ref. (39)
	g_{syn} (uS)	1.5e-3	Set to reproduce the bursting behavior in ref. (40)
	σ_w	1e-5	Set to induce synaptic current fluctuation of ±0.2 nA
DCN→ION (dentato-rubro-	$\tau_1^{DCN\rightarrow ION}$ (ms)	2	Refs. (17, 41)
	$\tau_2^{DCN\rightarrow ION}$ (ms)	10	Refs. (17, 41)
	E_{syn} (mV)	0	
	Δt (ms)	15	Refs. (17, 41)

olivary pathway)	g_{syn} (uS)	8e-6	Refs. (17, 41)
	σ_w	1e-12	Set to induce ±2e-5 pA synaptic current fluctuation
NO→ION	$\tau_1^{NO\rightarrow ION}$ (ms)	40	Refs. (17, 27, 42)
	$\tau_2^{NO\rightarrow ION}$ (ms)	180	Refs. (17, 27, 42)
	E_{syn} (mV)	-65	Ref. (27)
	Δt (ms)	45	Refs. (17, 27)
	g_{syn} (uS)	3e-5	Refs. (17, 27)
	σ_w	1e-12	Set to induce ±2e-5 pA synaptic current fluctuation
PP→ION	$\tau_1^{PP\rightarrow ION}$ (ms)	2	Refs. (17, 41)
	$\tau_2^{PP\rightarrow ION}$ (ms)	10	Refs. (17, 41)
	E_{syn} (mV)	0	
	g_{syn} (uS)	1.5e-5	Set to adjust the *in vivo* firing rate as in ref. (1)
PYN→PYN	E_{syn} (mV)	0	Ref. (24)
	g_{syn} (uS)	2.7e-2×w, $w \sim \mathcal{N}(\mu, \sigma^2)$, μ=1, σ=0.2	Modified from ref. (24)
	σ_w	1e-5	Set to induce ±5.0 pA synaptic current fluctuation
FSI→FSI	E_{syn} (mV)	-80	Ref. (24)
	g_{syn} (uS)	1.5e-3	Modified from ref. (24)
	σ_w	1e-5	Set to induce ±0.3 pA synaptic current fluctuation
FSI→PYN	E_{syn} (mV)	-80	Ref. (24)
	g_{syn} (uS)	2.2e-2×w, $w \sim \mathcal{N}(\mu, \sigma^2)$, μ=1, σ=0.16	Modified from ref. (24)
	σ_w	1e-5	Set to induce ±4.0 pA synaptic current fluctuation
PYN→FSI	E_{syn} (mV)	0	Ref. (24)
	g_{syn} (uS)	2.5e-3	Modified from ref. (24)
	σ_w	1e-5	Set to induce ±0.5 pA synaptic current fluctuation
PP→PYN	$\tau^{PP\rightarrow PYN}$ (ms)	3	Modified from ref. (24)
	E_{syn} (mV)	0	Ref. (24)
	g_{syn} (uS)	2.2e-3×w, $w \sim \mathcal{N}(\mu, \sigma^2)$, μ=1, σ=0.5	Set to adjust the *in vivo* firing rate as in ref. (43)
TC→PYN	$\tau^{Vim\rightarrow PYN}$ (ms)	5.26	Ref. (24)
	E_{syn} (mV)	0	Ref. (24)
	Δt (ms)	1	
	g_{syn} (uS)	1.5e-2×w, $w \sim \mathcal{N}(\mu, \sigma^2)$, μ=1, σ=0.25	Refs. (24, 43)
	σ_w	1e-6	Set to induce ±0.2 nA synaptic current fluctuation
PYN→TC	$\tau^{PYN\rightarrow Vim}$ (ms)	5.26	Ref. (24)
	E_{syn} (mV)	0	Ref. (24)
	Δt (ms)	1	
	g_{syn} (uS)	9e-4×w, $w \in$ [0.64,1.36,0.60,1.53]	Modified from ref. (24)
	σ_w	1e-6	Set to induce ±0.2 nA synaptic current fluctuation
TC→FSI	$\tau^{Vim\rightarrow FSI}$ (ms)	5.26	Ref. (24)
	E_{syn} (mV)	0	Ref. (24)
	Δt (ms)	2	
	g_{syn} (uS)	9e-4	Modified from ref. (24)
	σ_w	1e-6	Set to induce ±0.2 nA synaptic current fluctuation
PYN→GrC (AMPA)	E_{syn} (mV)	0	Ref. (10)
	Δt (ms)	4	Ref. (10, 15)

	g_{syn} (nS)	3.48	Modified from ref. (10)
PYN→GrC (NMDA)	E_{syn} (mV)	0	Ref. (10)
	Δt (ms)	4	Ref. (10, 15)
	g_{syn} (nS)	0.348	Modified from ref. (10)
PYN→GoC	E_{syn} (mV)	0	Ref. (10)
	Δt (ms)	4	Ref. (10, 15)
	g_{syn} (nS)	50	Modified from ref. (10)
GrC→GoC	E_{syn} (mV)	0	Ref. (10)
	Δt (ms)	1	Ref. (10)
	g_{syn} (nS)	300	Modified from ref. (10)
GrC→STC	E_{syn} (mV)	0	Ref. (10)
	Δt (ms)	1	Ref. (10)
	g_{syn} (nS)	30	Modified from ref. (10)
GoC→GrC	E_{syn} (mV)	-65	Ref. (10)
	Δt (ms)	0.5	Ref. (10)
	g_{syn} (nS)	6	Modified from ref. (10)
STC→GoC	E_{syn} (mV)	-65	Ref. (10)
	Δt (ms)	1	Ref. (10)
	g_{syn} (nS)	12.5	Modified from ref. (10)
GrC→PC	$\tau_1^{GrC\rightarrow PC}$ (ms)	1.2	Ref. (10, 44)
	$\tau_2^{GrC\rightarrow PC}$ (ms)	14	Ref. (10, 44)
	E_{syn} (mV)	0	
	Δt (ms)	$\Delta t \sim \mathcal{U}(0, 10)$	Estimated from (45)
	g_{syn} (uS)	3.27e-5×w, $w \sim \mathcal{N}(\mu, \sigma^2)$, μ=1, σ=0.5	Set to match the *in vivo* firing rate as in ref. (2)
	σ_w	5e-9	Set to induce ±0.1 pA synaptic current fluctuation
PYN→DCN (AMPA)	$\tau^{PYN\rightarrow DCN\ (AMPA)}$ (ms)	1	Ref. (16)
	E_{syn} (mV)	0	
	Δt (ms)	1.7	Ref. (16)
	g_{syn} (uS)	2.1e-4	Relative amplitude vs NMDA: ref. (16); set to match *in vivo* firing rate in ref. (2)
	σ_w	1e-10	Set to induce ±5.5e-5 pA current fluctuation
PYN→DCN (NMDA)	$\tau_1^{PYN\rightarrow DCN\ (NMDA)}$ (ms)	1	Ref. (16)
	$\tau_2^{PYN\rightarrow DCN\ (NMDA)}$ (ms)	6	Ref. (16)
	E_{syn} (mV)	0	
	Δt (ms)	1.7	Ref. (46)
	g_{syn} (uS)	1.26e-4	Set to match *in vivo* firing rate in ref. (2)
	σ_w	1e-10	Set to induce ±5.5e-5 pA current fluctuation

Table S2. Synaptic mechanisms used in the model. *Legend*: CS = complex spike; GrC = granule cell; GoC = Golgi cell; STC = stellate cell. PP = presynaptic Poisson process source input to ION or PYN neurons. w ~$\mathcal{N}(\mu, \sigma^2)$, is the Gaussian distribution with mean μ and standard deviation σ.